Comput. Methods Appl. Mech. Engrg. 198 (2009) 2067–2077

Contents lists available at ScienceDirect

Comput. Methods Appl. Mech. Engrg.

journal homepage: www.elsevier.com/locate/cma

A numerical upscaling procedure to estimate effective plane wave and shear moduli in heterogeneous fluid-saturated poroelastic media

Juan E. Santos [a,b,*], J. Germán Rubino [a], Claudia L. Ravazzoli [a]

[a] CONICET, Fac. de Cs. Astronómicas y Geofísicas, Universidad Nacional de La Plata, Paseo del Bosque s/n, B1900FWA – La Plata, Argentina
[b] Department of Mathematics, Purdue University, 150 N. University Street, West Lafayette, IN 47907-2067, USA

ARTICLE INFO

Article history:
Received 12 January 2008
Received in revised form 18 November 2008
Accepted 3 February 2009
Available online 15 February 2009

Keywords:
Attenuation and dispersion
Poroelasticity
Viscoelasticity
Finite element methods
Monte Carlo method

ABSTRACT

An important loss effect in heterogeneous poroelastic Biot media is the dissipation mechanism due to wave-induced fluid flow caused by mesoscopic scale heterogeneities, which are larger than the pore size but much smaller than the predominant wavelengths of the fast compressional and shear waves. These heterogeneities can be due to local variations in lithological properties or to patches of immiscible fluids. For example, a fast compressional wave traveling across a porous rock saturated with water and patches of gas induces a smaller fluid-pressure in the gas patches than in the water-saturated parts of the material. This in turn generates fluid flow and slow Biot waves which diffuse away from the gas–water interfaces generating significant energy losses and velocity dispersion. To perform numerical simulations using Biot's equations of motion, it would be necessary to employ extremely fine meshes to properly represent these mesoscopic heterogeneities and their attenuation effects on the fast waves. An alternative approach to model wave propagation in these type of Biot media is to employ a numerical upscaling procedure to determine *effective* complex P-wave and shear moduli defining locally a viscoelastic medium having in the average the same properties than the original Biot medium. In this work the complex P-wave and shear moduli in heterogeneous fluid-saturated porous media are obtained using numerical *gedanken* experiments in a Monte Carlo fashion. The experiments are defined as local boundary value problems on a reference representative volume of bulk material containing stochastic heterogeneities characterized by their statistical properties. These boundary value problems represent compressibility and shear tests needed to determine these moduli for a given realization. The average and variance of the phase velocities and quality factors associated with these moduli are obtained by averaging over realizations of the stochastic parameters. The Monte Carlo realizations were stopped when the variance of the computed quantities stabilized at an almost constant value. The approximate solution of the local boundary value problems was obtained using a Galerkin finite element procedure, and the method was validated by reproducing known solutions in the case of periodic layered media. For the spatial discretization, standard bilinear finite element spaces are employed for the solid phase, while for the fluid phase the vector part of the Raviart–Thomas–Nedelec mixed finite element space of order zero was used. Results on the uniqueness of the continuous and discrete problems as well as optimal *a priori* error estimates for the Galerkin finite element procedure are derived. Numerical experiments showing the implementation of the procedure to estimate the average and variance of the fast compressional and shear phase velocities and inverse quality factors in these kind of highly heterogeneous fluid-saturated porous media are presented.

1. Introduction

A major cause of the attenuation levels observed in seismic data from sedimentary regions is the mesoscopic loss mechanism, caused by heterogeneities in the rock and fluid properties greater than the pore size but much smaller than the wavelengths of the fast compressional and shear waves. When a compressional wave travels through an heterogeneous fluid-saturated porous material, the different regions may undergo different strains and fluid pressures. This in turn generates fluid flow and diffusive Biot slow waves inducing energy losses and velocity dispersion. The study of this attenuation mechanism has motivated the interest and research of many authors in this field, such as [22,23,8,17,14,5], among others.

* Corresponding author. Address: CONICET, Fac. de Cs. Astronómicas y Geofísicas, Universidad Nacional de La Plata, Paseo del Bosque s/n, B1900FWA – La Plata, Argentina. Fax: +54 221 4236591.
E-mail addresses: santos@fcaglp.unlp.edu.ar, santos@math.purdue.edu (J.E. Santos).

0045-7825/$ - see front matter © 2009 Elsevier B.V. All rights reserved.
doi:10.1016/j.cma.2009.02.003

Mesoscopic effects have been analyzed by using numerical simulation of wave propagation employing Biot's equations of motion [12,19]. One major problem of this approach is that even in the hypothetical case in which the exact spatial distribution of the different constituents were known, extremely fine meshes would be needed in order to properly define the mesoscopic scale heterogeneities, which makes this procedure computationally very expensive or even not feasible.

In this paper we present an alternative approach to overcome this difficulty. We propose to employ a finite element procedure combined with a Monte Carlo approach to obtain the *effective* complex P-wave and shear moduli in heterogeneous fluid-saturated porous solids with heterogeneities in the fluid and petrophysical properties described by stochastic fractals, allowing us to define an *effective* viscoelastic medium behaving in the average like the original medium.

The procedure consists in applying time-harmonic compressibility and shear stresses to numerical rock samples associated with a given realization of the stochastic parameters at a finite number of oscillatory frequencies. The complex moduli are calculated by defining locally an *equivalent* viscoelastic solid having the same attenuation and velocity dispersion than the original fluid-saturated porous rock. Biot's theory [3] is used to model the response of the heterogeneous material to the applied stresses. The procedure is a generalization of the ideas presented in [22,23] to explain the attenuation effects suffered by compressional waves travelling in partially saturated rocks for the idealized cases of alternating layers saturated either with gas or water or for a water-saturated rock containing spherical gas pockets.

For each realization of the stochastic parameters, the complex moduli are obtained by solving numerically Biot's equations of motion in the space-frequency domain employing a finite element procedure, with appropriate boundary conditions representing compressibility and shear *gedanken* laboratory experiments. These complex moduli in turn allow us to obtain the corresponding *equivalent* compressional and shear phase velocities and quality factors for each frequency and realization.

The statistical properties of the computed *equivalent* phase velocities and inverse quality factors were obtained by averaging over the realizations of the stochastic parameters. The Monte Carlo realizations were stopped when the variance of the computed quantities stabilized at an almost constant value, allowing us to determine *effective* phase velocities and quality factors of the fast compressional and shear waves associated with an *effective* viscoelastic medium behaving in the average as our original highly heterogeneous fluid filled porous medium.

The numerical procedure presented can be regarded as an upscaling method to obtain the effect of the mesoscopic scale heterogeneities on the macroscale. For the compressional case the algorithm was validated comparing the results with those obtained using a White's model which is valid for alternating layers of two fluid-saturated porous sandstones [23]. For the shear case, the algorithm was checked to yield the real shear modulus for the case of uniform either gas or water saturation at the zero frequency limit.

The organization of the paper is as follows. In Section 2, a review of Biot's theory of wave propagation in fluid-saturated poroelastic media is presented and the local boundary value problems associated with the numerical *gedanken* experiments are formulated. Section 3, presents a variational formulation of the boundary value problems as well as uniqueness results. In Section 4, the finite element procedures to be employed are formulated. Section 5, is devoted to the derivation of *a priori* error estimates for the numerical procedure, and Section 6 presents the Monte Carlo approach to determine the *effective* moduli for the heterogeneous poroelastic fluid filled material with heterogeneities described by fractal spectral density distributions. Section 7, presents numerical experiments showing the validation of the procedure and its application to determine the *effective* compressional and shear phase velocities and inverse quality factors in the cases of a sandstone with patchy gas–water saturation and a partially saturated shale–sandstone mixture. Finally, the conclusions are drawn in Section 8.

2. Review of Biot's theory

We consider a porous solid saturated by a single phase, compressible viscous fluid and assume that the whole aggregate is isotropic. Let $u^s = (u_i^s)$ and $\tilde{u}^f = (\tilde{u}_i^f),\ i = 1,\ldots,E$ denote the averaged displacement vectors of the solid and fluid phases, respectively, where E denotes the Euclidean dimension. Also let

$$u^f = \phi(\tilde{u}^f - u^s),$$

be the average relative fluid displacement per unit volume of bulk material, with ϕ denoting the effective porosity. Set $u = (u^s, u^f)$ and note that

$$\xi = -\nabla \cdot u^f,$$

represents the change in fluid content.

Let $\varepsilon_{ij}(u^s)$ be the strain tensor of the solid. Also, let $\sigma_{ij}, i,j = 1,\ldots,E$, and p_f denote the stress tensor of the bulk material and the fluid pressure respectively. Following [3], the stress–strain relations can be written in the form:

$$\sigma_{ij}(u) = 2\mu\varepsilon_{ij}(u^s) + \delta_{ij}(\lambda_c \nabla \cdot u^s - \alpha K_{av}\xi), \tag{1a}$$

$$p_f(u) = -\alpha K_{av}\nabla \cdot u^s + K_{av}\xi. \tag{1b}$$

The coefficient μ is the shear modulus of the bulk material, considered to be equal to the shear modulus of the dry matrix. Also

$$\lambda_c = K_c - \frac{2}{E}\mu, \tag{2}$$

with K_c being the bulk modulus of the saturated material. Following [20,10] the coefficients in (1) can be obtained from the relations

$$\alpha = 1 - \frac{K_m}{K_s}, \quad K_{av} = \left(\frac{\alpha - \phi}{K_s} + \frac{\phi}{K_f}\right)^{-1}, \quad K_c = K_m + \alpha^2 K_{av}, \tag{3}$$

where K_s, K_m and K_f denote the bulk modulus of the solid grains composing the solid matrix, the dry matrix and the saturant fluid, respectively. The coefficient α is known as the effective stress coefficient of the bulk material.

2.1. The equations of motion

Let ρ_s and ρ_f denote the mass densities of the solid grains and the fluid and let

$$\rho_b = (1-\phi)\rho_s + \phi\rho_f,$$

denote the mass density of the bulk material. Let the positive definite matrix $\mathscr{P}$ and the nonnegative matrix $\mathscr{B}$ be defined by

$$\mathscr{P} = \begin{pmatrix} \rho_b I & \rho_f I \\ \rho_f I & mI \end{pmatrix}, \quad \mathscr{B} = \begin{pmatrix} 0I & 0I \\ 0I & bI \end{pmatrix}.$$

Here I denotes the identity matrix in $R^{E\times E}$. The mass coupling coefficient m represents the inertial effects associated with dynamic interactions between the solid and fluid phases, while the coefficient b includes the viscous coupling effects between such phases. They are given by the relations

$$b = \frac{\eta}{k}, \quad m = \frac{S\rho_f}{\phi}, \quad S = \frac{1}{2}\left(1 + \frac{1}{\phi}\right), \tag{4}$$

where η is the fluid viscosity and k the absolute permeability. S is known as the structure or tortuosity factor. Next, let $\mathscr{L}(u)$ be the second order differential operator defined by

$$\mathscr{L}(u) = \left(\nabla \cdot \sigma(u), -\nabla p_f(u)\right).$$

Then if $\omega = 2\pi f$ is the angular frequency, in the absence of body forces Biot's equations of motion, stated in the space-frequency domain are [1,2]

$$-\omega^2 \mathscr{P} u(x,\omega) + i\omega \mathscr{B} u(x,\omega) - \mathscr{L}(u(x,\omega)) = 0. \tag{5}$$

It was shown by Biot [1,2] that in this type of media two compressional waves, denoted here as P1 and P2, and one shear or S wave can propagate. The P1 and S waves correspond to the classical compressional and shear waves propagating in elastic or viscoelastic isotropic solids. The additional P2 slow mode is a wave strongly attenuated in the low-frequency range, associated with the motion out of phase of the solid and fluid phases.

2.2. The numerical gedanken experiments

Field measurements show that permeability values in reservoir rocks have a high degree of spatial variability and exhibit long range correlations. It is also known that these permeability fluctuations are well described by stochastic fractals [7].

It is also the case that in hydrocarbon reservoirs, regions of non-uniform patchy saturation occur at gas–oil and gas–water contacts. By using computerized tomography scans (CT scans) it is possible to visualize the fluid distribution and spatial heterogeneities in real rocks [4]. Helle et al. [12] used fractal models as the von Karman correlation function [9] calibrated by the CT scans to perform numerical wave propagation simulations using Biot's equations of motion.

These are two examples of highly heterogeneous saturated porous media where the sizes of the heterogeneities are small as compared with the wavelengths of the fast compressional and shear waves. Consequently, solving Biot's equations of motion in these type of media can be computationally very expensive or even not feasible due to the extremely fine meshes that would be needed to define the local (mesoscopic scale) heterogeneities.

Thus the objective of this work is to define a numerical upscaling procedure to determine in a statistical framework the complex plane wave and shear moduli associated with a representative sample of our heterogenous material. This procedure will allow in turn to define an *effective* viscoelastic solid where its complex moduli carry over to the macroscale the effects due to the mesoscopic scale heterogeneities.

For that purpose, the space-frequency formulation of Biot's equations of motion combined with a Monte Carlo approach is particularly convenient, since can handle complex geometries and deal with extremely large variability in the stochastic parameters. The proposed algorithm is described as follows.

Eq. (5) will be solved in the 2D case on a reference square $\Omega = (0,L)^2$ with boundary Γ in the (x,y)-plane containing a representative set of stochastic heterogeneities with a given distribution and size. Thus, in a Monte Carlo fashion, (5) will be solved for a finite number of frequencies in the range of interest and for a large number of realizations of the stochastic parameters, with boundary conditions representing compressibility and shear tests that after averaging over realizations will yield the moments (average and variance in this case) of the phase velocities and inverse of quality factors of our heterogeneous material. To stop the Monte Carlo procedure, a criteria based on the stabilization of the variance of the computed phase velocities and inverse quality factors was employed. This criteria was also used in [11] to obtain the moments of the computed variables for stochastic modeling of variably saturated transient flow in fractal soils.

Set $\Gamma = \Gamma^L \cup \Gamma^B \cup \Gamma^R \cup \Gamma^T$, where

$$\Gamma^L = \{(x,y) \in \Gamma : x = 0\}, \quad \Gamma^R = \{(x,y) \in \Gamma : x = L\},$$

$$\Gamma^B = \{(x,y) \in \Gamma : y = 0\}, \quad \Gamma^T = \{(x,y) \in \Gamma : y = L\}.$$

Denote by ν the unit outer normal on Γ and let χ be a unit tangent on Γ so that $\{\nu,\chi\}$ is an orthonormal system on Γ.

For obtaining the complex plane wave modulus of our fluid-saturated porous medium, let us consider the solution of (5) with the following boundary conditions

$$\sigma(u)\nu \cdot \nu = -\Delta P, \quad (x,y) \in \Gamma^T, \tag{6}$$

$$\sigma(u)\nu \cdot \chi = 0, \quad (x,y) \in \Gamma^T, \tag{7}$$

$$\sigma(u)\nu \cdot \chi = 0, \quad (x,y) \in \Gamma^L \cup \Gamma^R, \tag{8}$$

$$u^s \cdot \nu = 0, \quad (x,y) \in \Gamma^L \cup \Gamma^R, \tag{9}$$

$$u^s = 0, \quad (x,y) \in \Gamma^B, \tag{10}$$

$$u^f \cdot \nu = 0, \quad (x,y) \in \Gamma. \tag{11}$$

For this set of boundary conditions the solid is not allowed to move on the bottom boundary Γ^B, the fluid is not allowed to flow out of the sample, a uniform compression is applied on the boundary Γ^T and no tangential external forces are applied on the boundaries $\Gamma^L \cup \Gamma^R \cup \Gamma^T$. These boundary conditions can be associated with a laboratory experiment for a periodic sample obtained by a mirror reflection with respect to the x-axis of the domain Ω, enclosing the periodic sample in a thin impermeable jacket and applying a uniform compression on the boundary Γ^T and its corresponding image boundary after the indicated reflection. In the case of periodic layered media, this experiment mimics exactly the one described by White et al. in [23]. In Section 3, we show that uniqueness holds for (5) with the boundary conditions (6)–(11) for $\omega > 0$ sufficiently small in the sense that ω satisfies the condition (34).

Denoting by V the original volume of the sample, its (complex) oscillatory volume change, $\Delta V(\omega)$, allows us to define the *equivalent* undrained complex plane wave modulus $\overline{M_c}(\omega)$, by using the relation

$$\frac{\Delta V(\omega)}{V} = -\frac{\Delta P}{\overline{M_c}(\omega)}, \tag{12}$$

valid for a viscoelastic homogeneous medium in the quasistatic case.

After solving (5) with the boundary conditions (6)–(11), the vertical displacements $u_y^s(x,L,\omega)$ on Γ^T allow us to obtain an average vertical displacement $u_y^{s,T}(\omega)$ suffered by the boundary Γ^T. Then, for each frequency ω, the volume change produced by the compressibility test can be approximated by $\Delta V(\omega) \approx L u_y^{s,T}(\omega)$, which enable us to compute the *equivalent* complex plane wave modulus $\overline{M_c}(\omega)$ by using the relation (12). The corresponding complex compressional velocity is

$$V_{pc}(\omega) = \sqrt{\frac{\overline{M_c}(\omega)}{\bar{\rho}_b}}, \tag{13}$$

where $\bar{\rho}_b$ is the average bulk density of the sample.

The following relations allow us to estimate the *equivalent* compressional phase velocity $V_p(\omega)$ and quality factor $Q_p(\omega)$ in the form [19]:

$$V_p(\omega) = \left[Re\left(\frac{1}{V_{pc}(\omega)}\right)\right]^{-1}, \quad \frac{1}{Q_p(\omega)} = \frac{\mathrm{Im}(V_{pc}(\omega)^2)}{\mathrm{Re}(V_{pc}(\omega)^2)} \tag{14}$$

For obtaining the *equivalent* complex shear modulus of our fluid-saturated porous medium, let us consider the solution of (5) with the following boundary conditions

$$-\sigma(u)v = g, \quad (x,y) \in \Gamma^T \cup \Gamma^L \cup \Gamma^R, \tag{15}$$

$$u^s = 0, \quad (x,y) \in \Gamma^B, \tag{16}$$

$$u^f \cdot v = 0, \quad (x,y) \in \Gamma, \tag{17}$$

where

$$g = \begin{cases} (0,\Delta p), & (x,y) \in \Gamma^L, \\ (0,-\Delta p), & (x,y) \in \Gamma^R, \\ (-\Delta p, 0), & (x,y) \in \Gamma^T. \end{cases}$$

Uniqueness for (5) with the boundary conditions (15)–(17) holds for any $\omega > 0$ satisfying the condition (34) (c.f. Section 3). The change in shape of the rock sample allows to recover its *equivalent* complex shear modulus $\bar{\mu}_c(\omega)$ by using the relation

$$tg(\theta(\omega)) = \frac{\Delta p}{\bar{\mu}_c(\omega)}, \tag{18}$$

where $\theta(\omega)$ is the departure angle between the original positions of the lateral boundaries and those after applying the shear stresses (see, for example, [13]). Eq. (18) holds for this experiment in a viscoelastic homogeneous media in the quasistatic approximation.

The horizontal displacements $u_x^s(x,L,\omega)$ at the top boundary Γ^T allow us to obtain, for each frequency, an average horizontal displacement $u_x^{s,T}(\omega)$ suffered by the boundary Γ^T. This average value allows us to approximate the change in shape suffered by the sample, given by $tg(\theta(\omega)) \approx u_x^{s,T}(\omega)/L$, which from (18) let us estimate $\bar{\mu}_c(\omega)$.

The complex shear velocity is given by

$$V_{sc}(\omega) = \sqrt{\frac{\bar{\mu}_c(\omega)}{\bar{\rho}_b}} \tag{19}$$

and the *equivalent* shear phase velocity $V_s(\omega)$ and (inverse) quality factor $Q_s(\omega)$ are estimated using the relations

$$V_s(\omega) = \left[\mathrm{Re}\left(\frac{1}{V_{sc}(\omega)}\right)\right]^{-1}, \quad \frac{1}{Q_s(\omega)} = \frac{\mathrm{Im}(V_{sc}(\omega)^2)}{\mathrm{Re}(V_{sc}(\omega)^2)}. \tag{20}$$

3. A variational formulation

In order to state a variational formulation for (5) and either (6)–(11) or (15)–(17) we need to introduce some notation. For $X \subset \mathbb{R}^d$ with boundary ∂X, let $(\cdot,\cdot)_X$ and $\langle\cdot,\cdot\rangle_{\partial X}$ denote the complex $L^2(X)$ and $L^2(\partial X)$ inner products for scalar, vector, or matrix valued functions. Also, for $s \in \mathbb{R}$, $\|\cdot\|_{s,X}$ and $|\cdot|_{s,X}$ will denote the usual norm and seminorm for the Sobolev space $H^s(X)$. In addition, if $X = \Omega$ or $X = \Gamma$, the subscript X may be omitted such that $(\cdot,\cdot) = (\cdot,\cdot)_\Omega$ or $\langle\cdot,\cdot\rangle = \langle\cdot,\cdot\rangle_\Gamma$. Also, let us introduce the spaces

$$H_{0,B}^{1,P}(\Omega) = \{v \in [H^1(\Omega)]^2 : v \cdot \nu = 0 \text{ on } \Gamma^L \cup \Gamma^R, v = 0 \text{ on } \Gamma^B\},$$

$$H_{0,B}^{1,T}(\Omega) = \{v \in [H^1(\Omega)]^2 : v = 0 \text{ on } \Gamma^B\},$$

$$H_0(\mathrm{div};\Omega) = \{v \in [L^2(\Omega)]^2 : \nabla \cdot v \in L^2(\Omega), v \cdot \nu = 0 \text{ on } \Gamma\},$$

and

$$H_0^1(\mathrm{div};\Omega) = \{v \in [H^1(\Omega)]^2 : \nabla \cdot v \in H^1(\Omega), v \cdot \nu = 0 \text{ on } \Gamma\}.$$

The spaces $H_{0,B}^{1,P}$ and $H_{0,B}^{1,T}$ are closed subspaces of $H^1(\Omega)$. Also, the norm in $H_0(\mathrm{div};\Omega)$ is given by

$$\|v\|_{H(\mathrm{div};\Omega)} = \left[\|v\|_0^2 + \|\nabla \cdot v\|_0^2\right]^{1/2}.$$

Let us introduce the spaces

$$\mathscr{V}^{(P)} = \left[H_{0,B}^{1,P}(\Omega)\right]^2 \times H_0(\mathrm{div};\Omega), \quad \mathscr{V}^{(T)} = \left[H_{0,B}^{1,T}(\Omega)\right]^2 \times H_0(\mathrm{div};\Omega).$$

Then multiply Eq. (5) by $v = (v^s, v^f) \in \mathscr{V}^{(P)}$, use integration by parts and apply the boundary conditions (6)–(8) to see that the solution $u^{(P)} = (u^{(s,P)}, u^{(f,P)}) \in \mathscr{V}^{(P)}$ of (5) and (6)–(11) satisfies *the weak form*:

$$\Lambda(u^{(P)}, v) = -\langle \Delta P, v^s \cdot \nu \rangle_{\Gamma^T}, \quad \forall v = (v^s, v^f) \in \mathscr{V}^{(P)}, \tag{21}$$

where for $u = (u^s, u^f)$, $v = (v^s, v^f) \in [H^1(\Omega)]^2 \times H(\mathrm{div};\Omega)$, the bilinear form $\Lambda(u,v)$ is defined by

$$\begin{aligned} \Lambda(u,v) &= -\omega^2(\mathscr{P}u, v) + i\omega(\mathscr{B}u, v) + \sum_{l,m}(\tau_{lm}(u), \varepsilon_{lm}(v^s)) \\ &\quad - (p_f(u), \nabla \cdot v^f) \\ &= -\omega^2(\mathscr{P}u, v) + i\omega\left(bu^f, v^f\right) + (\mathbf{D}\tilde{\epsilon}(u), \tilde{\epsilon}(v)). \end{aligned} \tag{22}$$

In (22), the matrix $\mathbf{D}$ and the column vector $\tilde{\varepsilon}((u))$ are defined by

$$\mathbf{D} = \begin{pmatrix} \lambda_c + 2\mu & \lambda_c & \alpha K_{av} & 0 \\ \lambda_c & \lambda_c + 2\mu & \alpha K_{av} & 0 \\ \alpha K_{av} & \alpha K_{av} & K_{av} & 0 \\ 0 & 0 & 0 & 4\mu \end{pmatrix}, \quad \tilde{\varepsilon}(u) = \begin{pmatrix} \varepsilon_{11}(u^s) \\ \varepsilon_{22}(u^s) \\ \nabla \cdot u^f \\ \varepsilon_{12}(u^s) \end{pmatrix}.$$

The term $(\mathbf{D}\tilde{\epsilon}(u), \tilde{\epsilon}(v))$ in (22) is associated with the strain energy of our system, so that the matrix $\mathbf{D}$ must be positive definite, with entries satisfying a set of conditions that can be determined as follows. Note that

$$\begin{aligned} (\mathbf{D}\tilde{\epsilon}(u), \tilde{\epsilon}(v)) = \int_\Omega \Big[&(\lambda_c + \mu)(\nabla \cdot u^s)^2 + \mu(\varepsilon_{11} - \varepsilon_{22})^2 + 4\mu\varepsilon_{12}^2 \\ &+ 2\alpha K_{av} \nabla \cdot u^s \nabla \cdot u^f + K_{av}(\nabla \cdot u^f)^2\Big] dx. \end{aligned} \tag{23}$$

Thus the choice $\nabla \cdot u^s = \nabla \cdot u^f = 0, \varepsilon_{11} = \varepsilon_{22}$ in (23) yields the condition

$$\mu > 0. \tag{24}$$

Next, the choice $\varepsilon_{11} = \varepsilon_{22}, \varepsilon_{12} = 0$ reduces (23) to

$$\begin{aligned} (\mathbf{D}\tilde{\epsilon}(u), \tilde{\epsilon}(v)) = \int_\Omega \Big[&(\lambda_c + \mu)(\nabla \cdot u^s)^2 + 2\alpha K_{av} \nabla \cdot u^s \nabla \cdot u^f \\ &+ K_{av}(\nabla \cdot u^f)^2\Big] dx. \end{aligned} \tag{25}$$

Thus we obtain the additional conditions

$$\lambda_c + \mu - \alpha^2 K_{av} > 0, \tag{26a}$$

$$K_{av} > 0. \tag{26b}$$

Hence (24), (26a) and (26b) are necessary and sufficient conditions for the matrix $\mathbf{D}$ to be positive definite. The condition (26a) imposes that the inverse of the jacketed compressibility be strictly positive. The jacketed compressibility test is an experiment in which a sample of bulk material is subjected to an hydrostatic compression while the fluid pressure is held constant, see [3].

Similarly, the solution $u^{(T)} = (u^{(s,T)}, u^{(f,T)}) \in \mathscr{V}^{(T)}$ of (5) and (15)–(17) satisfies *the weak form*:

$$\Lambda(u^{(T)}, v) = \langle g, v^s \rangle_{\Gamma^T}, \quad \forall v = (v^s, v^f) \in \mathscr{V}^{(T)}. \tag{27}$$

Existence of the solution of the boundary value problem (5) and either (6)–(11) or (15)–(17) and its variational formulations (21) or (27) will be assumed.

Let us analyze the uniqueness of the solution $u^{(P)}$ of (21). Set $\Delta P = 0$ and choose $v = u^{(P)}$ in (21) to obtain the equation

$$-\omega^2\left(\mathscr{P}u^{(P)}, u^{(P)}\right) + i\omega\left(bu^{(f,P)}, u^{(f,P)}\right) + (\mathbf{D}\tilde{\varepsilon}(u^{(P)}), \tilde{\varepsilon}(u^{(P)})) = 0. \tag{28}$$

Choose the imaginary part in (28) to see that

$$\|u^{(f,P)}\|_0^2 = 0. \tag{29}$$

Hence, (28) reduces to

$$-\omega^2\left(\rho_b u^{(s,P)}, u^{(s,P)}\right) + \left(\widehat{\mathbf{D}}\tilde{\tilde{\varepsilon}}(u^{(s,P)}), \tilde{\tilde{\varepsilon}}(u^{(s,P)})\right) = 0, \tag{30}$$

where

$$\widehat{\mathbf{D}} = \begin{pmatrix} \lambda_c + 2\mu & \lambda_c & 0 \\ \lambda_c & \lambda_c + 2\mu & 0 \\ 0 & 0 & 4\mu \end{pmatrix}, \quad \tilde{\tilde{\varepsilon}}(u^{(s,P)}) = \begin{pmatrix} \varepsilon_{11}(u^{(s,P)}) \\ \varepsilon_{22}(u^{(s,P)}) \\ \varepsilon_{12}(u^{(s,P)}) \end{pmatrix}.$$

Next, recall that for any v vanishing on a subset of positive measure of Γ, (in our case Γ^B) using Korn's second inequality [16] it can be shown that [6]

$$|||v||| = \left(\sum_{kl}\int_\Omega |\varepsilon_{kl}(v)|^2 d\Omega\right)^{1/2} \tag{31}$$

defines on $H^{1,P}_{0,B}(\Omega)$ a norm equivalent to the H^1-norm, so that for some positive constants C_1, C_2,

$$C_1\|v\|_1 \leqslant |||v||| \leqslant C_2\|v\|_1, \quad \forall v \in H^{1,P}_{0,B}(\Omega). \tag{32}$$

Consequently, if $\lambda_{min}(\widehat{\mathbf{D}})$ is the minimum eigenvalues of the matrix $\widehat{\mathbf{D}}$ and ρ_b^{max} the maximum value of $\rho_b(x,y)$, it follows from (30) that

$$\begin{aligned} 0 &\geqslant -\omega^2\rho_b^{max}\|u^{(s,P)}\|_o^2 + \lambda_{min}(\widehat{\mathbf{D}})C_1^2\|u^{(s,P)}\|_1^2 \\ &\geqslant \lambda_{min}(\widehat{\mathbf{D}})C_1^2\|\nabla u^{(s,P)}\|_0^2 + \left(\lambda_{min}(\widehat{\mathbf{D}})C_1^2 - \omega^2\rho_b^{max}\right)\|u^{(s,P)}\|_0^2 \\ &\geqslant \lambda_{min}(\widehat{\mathbf{D}})C_1^2\|\nabla u^{(s,P)}\|_0^2, \end{aligned} \tag{33}$$

provided ω satisfies the condition

$$\omega < C_1\sqrt{\frac{\lambda_{min}(\widehat{\mathbf{D}})}{\rho_b^{max}}}. \tag{34}$$

Next, recall that for any $v \in H^{1,P}_{0,B}(\Omega)$ Poincare's inequality holds, *i.e.*,

$$\|v\|_0 \leqslant C_3\|\nabla v\|_0. \tag{35}$$

Hence combining (33) and (35) it follows that

$$\|u^{(s,P)}\|_0 = 0. \tag{36}$$

Thus (29) and (36) yield uniqueness for the solution of (21) for $\omega > 0$ satisfying (34).

Uniqueness of the solution $u^{(T)}$ of (27) can be demonstrated in analogous fashion, with identical condition as in (34) on the range of frequencies. Hence we conclude the validity of the following theorem.

Theorem 1. *The solution of problems (21) and (27) is unique for any $\omega > 0$ satisfying the condition (34).*

4. The finite element procedures

Let $\mathscr{T}^h(\Omega)$ be a non-overlapping partition of Ω into rectangles Ω_j of diameter bounded by h such that $\overline{\Omega} = \cup_{j=1}^J \overline{\Omega}_j$. Different finite element spaces, denoted $\mathscr{N}^{h,P}_{0,B} \subset H^{1,P}_{0,B}(\Omega)$ and $\mathscr{N}^{h,T}_{0,B} \subset H^{1,T}_{0,B}(\Omega)$ were used to approximate the solid displacement vector for the compressibility and shear tests models, respectively. They are defined as follows

$$\begin{aligned} \mathscr{N}^{h,P}_{0,B} = \{v : v|_{\Omega_j} \in P_{1,1}\times P_{1,1}, v\cdot\nu = 0 \text{ on } \Gamma^L\cup\Gamma^R, v \\ = 0 \text{ on } \Gamma^B\} \cap [C^0(\overline{\Omega})]^2, \end{aligned}$$

$$\mathscr{N}^{h,T}_{0,B} = \{v : v|_{\Omega_j} \in P_{1,1}\times P_{1,1}, v = 0 \text{ on } \Gamma^B\} \cap [C^0(\overline{\Omega})]^2,$$

where $P_{1,1}$ denotes the polynomials of degree not greater than 1 on each variable.

To approximate the fluid displacement a closed subspace of the vector part of the Raviart–Thomas–Nedelec space of zero order, denoted $\mathscr{W}^h_0$, was employed [18,15]. It is defined as

$$\mathscr{W}^h_0 = \{v : v|_{\Omega_j} \in P_{1,0}\times P_{0,1}, v\cdot\nu = 0 \text{ on } \Gamma\}.$$

Let

$$\Pi_h^{(P)} : \left[H^2(\Omega)\cap H^{1,P}_{0,B}(\Omega)\right]^2 \to \mathscr{N}^{h,P}_{0,B}, \quad \Pi_h^{(T)} : \left[H^2(\Omega)\cap H^{1,T}_{0,B}(\Omega)\right]^2 \to \mathscr{N}^{h,T}_{0,B}$$

be the interpolant operators associated with the spaces $\mathscr{N}^{h,P}_{0,B}$ and $\mathscr{N}^{h,T}_{0,B}$, respectively. More specifically, the degress of freedom associated with $\Pi_h^{(P)}\varphi$ are the vertices of the rectangles Ω_j and if b is a common node of the adjacent rectangles Ω_j and Ω_k then $(\Pi_h^{(P)}\varphi)_j(b) = (\Pi_h^{(P)}\varphi)_k(b)$, where $(\Pi_h^{(P)}\varphi)_j$ denotes the restriction of the interpolant $\Pi_h^{(P)}\varphi$ of φ to Ω_j.

Also, let

$$Q^h : H^1_0(\mathrm{div};\Omega) \to \mathscr{W}^h_0 \tag{37}$$

be the projection defined by

$$\left\langle (Q^h\psi - \psi)\cdot\nu, 1\right\rangle_B = 0, \quad B = \partial\Omega_j\cap\partial\Omega_k \text{ or } B = \partial\Omega_j\cap\partial\Omega.$$

It is well known that, for all $\varphi \in [H^2(\Omega)\cap H^{1,P}_{0,B}(\Omega)]^2$, $\psi \in [H^2(\Omega)\cap H^{1,T}_{0,B}(\Omega)]^2$ and $\eta \in H^1_0(\mathrm{div};\Omega)$ [6,15,18]

$$\|\varphi - \Pi_h^{(P)}\varphi\|_0 + h\|\varphi - \Pi_h^{(P)}\varphi\|_1 \leqslant Ch^2\|\varphi\|_2, \tag{37a}$$

$$\|\psi - \Pi_h^{(T)}\psi\|_0 + h\|\psi - \Pi_h^{(T)}\psi\|_1 \leqslant Ch^2\|\psi\|_2, \tag{37b}$$

$$\|\eta - Q^h\eta\|_0 \leqslant Ch\|\eta\|_1, \tag{37c}$$

$$\|\eta - Q^h\eta\|_{H(\mathrm{div};\Omega)} \leqslant Ch(\|\eta\|_1 + \|\nabla\cdot\eta\|_1). \tag{37d}$$

Let us define the finite element spaces

$$\mathscr{V}^{(h,P)} = \mathscr{N}^{h,P}_{0,B}\times\mathscr{W}^h_0, \quad \mathscr{V}^{(h,T)} = \mathscr{N}^{h,T}_{0,B}\times\mathscr{W}^h_0.$$

Then the finite element procedure to compute the approximate solution of (21) is defined as follows: find $u^{(h,P)} = (u^{(s,h,P)}, u^{(f,h,P)})^t \in \mathscr{V}^{h,P}$ such that

$$\Lambda(u^{(h,P)}, v) = -\langle\Delta P, v^s\cdot\nu\rangle_{\Gamma^T}, \quad v = \left(v^s, v^f\right) \in \mathscr{V}^{(h,P)}. \tag{38}$$

Also, the finite element procedure to compute the approximate solution of (27) is: find $u^{(h,T)} = (u^{(s,h,T)}, u^{(f,h,T)})^t \in \mathscr{V}^{(h,T)}$ such that

$$\Lambda(u^{(h,T)}, v) = \langle g, v^s\rangle_{\Gamma^T}, \quad v = \left(v^s, v^f\right) \in \mathscr{V}^{(h,T)}. \tag{39}$$

Since $u^{(h,P)} \in H^{1,P}_{0,B}, u^{(h,T)} \in H^{1,T}_{0,B}$, uniqueness for the discrete problems (38) and (39) follows with the same argument than for the continuous case provided the frequency ω satisfies the constraint (34). Existence follows from finite dimensionality. This result is stated in the following theorem.

Theorem 2. *There exists a unique solution of problems (38) and (39) for any $\omega > 0$ satisfying the condition (34).*

5. Error estimates for the finite element procedures

We will derive *a priori* error estimates for the procedure (38). The corresponding estimates for the procedure (39) follow with the same argument.

First, using (32) it follows that for $u = (u^s, u^f) \in \mathscr{V}^P$, the bilinear form Λ satisfies the Garding-type inequality

$$\begin{aligned} \mathrm{Re}(\Lambda(u,u)) &\geqslant \lambda_{min}(\mathbf{D})\left(|||u^s|||^2 + \|\nabla\cdot u^f\|_0^2\right) \\ &\quad - \omega^2\lambda^{max}(\mathscr{P})\left(\|u^s\|_0^2 + \|u^f\|_0^2\right) \\ &\geqslant C_4\left(\|u^s\|_1^2 + \|u^f\|_0^2 + \|\nabla\cdot u^f\|_0^2\right) - C_5(\omega)\|u^f\|_0^2, \end{aligned} \tag{40}$$

where

$$C_4 = \min\left(\frac{1}{2}\lambda_{\min}(\mathbf{D})C_1^2, \lambda_{min}(\mathbf{D})\right), \quad C_5(\omega) = \omega^2\lambda^{max}(\mathscr{P}) + \lambda_{\min}(\mathbf{D})$$

provided the frequency ω is small in the sense that satisfies the condition

$$\omega < \left(\frac{\lambda_{min}(\mathbf{D})C_1}{2\lambda^{max}(\mathscr{P})}\right)^{\frac{1}{2}}. \tag{41}$$

In the equations above $\lambda^{max}(\mathscr{P})$ denotes the maximum eigenvalue of the matrix $\mathscr{P}$.

Also, Λ is $\mathscr{V}^{(P)}$-continuous, i.e.,

$$|\Lambda(u,v)| \leqslant C_6(\omega)\big(\|u^s\|_1\|v^s\|_1 + \|\nabla\cdot u^s\|_0\|\nabla\cdot v^f\|_0 + \|u^f\|_0\|v^f\|_0\big)\forall u = (u^s,u^f), v = (v^s,v^f) \in \mathscr{V}^P. \tag{42}$$

Next set

$$e = u^{(h,P)} - u^{(P)} = (e^s, e^f)$$

and subtract (21) from (38) to obtain the error equation

$$\Lambda(e,v) = 0, \quad v = (v^s,v^f) \in \mathscr{V}^{(h,P)}. \tag{43}$$

Take $v = u^P - u^{h,P} + \psi - u^P, \psi = (\Pi_h^{(P)}u^{(s,P)}, Q_h u^{(f,P)}) \in \mathscr{V}^{(h,P)}$ in (43) to get

$$\Lambda((e^s,e^f),(e^s,e^f)) = \Lambda\Big((e^s,e^f),(u^{(s,P)} - \Pi_h^{(P)}u^{(s,P)}, u^{(f,P)} - Q_h^{(P)}u^{(f,P)})\Big). \tag{44}$$

Next take imaginary part in (44) an use (42) to see that

$$\begin{aligned}\mathrm{Im}(\Lambda(e,e)) &= \omega(be^f,e^f)\\ &\leqslant |\Lambda\Big((e^s,e^f),(u^{(s,P)} - \Pi_h^{(P)}u^{(s,P)}),(u^{(f,P)} - Q_h^{(P)}u^{(f,P)})\Big)|\\ &\leqslant C_6(\omega)\Big(\|e^s\|_1\|u^{s,P} - \Pi_h^{(P)}u^{(s,P)}\|_1\\ &\quad + \|\nabla\cdot e^f\|_0\|\nabla\cdot\big(u^{f,P} - Q_h u^{(f,P)}\big)\|_0\\ &\quad + \|e^f\|_0\|u^{f,P} - Q_h u^{(f,P)}\|_0\Big)\end{aligned} \tag{45}$$

Thus, using the approximating properties (37) in (45) yields the inequality

$$\|e^f\|_0^2 \leqslant C_7(\omega)h\big(\|e^s\|_1\|u^{s,P}\|_2 + \|\nabla\cdot e^{f,P}\|_0\|\nabla\cdot u^{(f,P)}\|_1 + \|e^f\|_0\|u^{(f,P)}\|_1\big). \tag{46}$$

Next, take real part in (44) and use the Garding inequality (40) and the estimates (42) and (46) to see that

$$\begin{aligned}&C_4\Big(\|e^s\|_1^2 + \|e^f\|_0^2 + \|\nabla\cdot e^f\|_0^2\Big)\\ &\leqslant \mathrm{Re}\Big(\Lambda\Big((e^s,e^f),(u^{(s,P)} - \Pi_h^{(P)}u^{(s,P)}),(u^{(f,P)} - Q_h^{(P)}u^{(f,P)})\Big)\Big) + C_5(\omega)\|e^f\|_0^2\\ &\leqslant C_8(\omega)\Big(\|e^s\|_1\|u^{s,P} - \Pi_h^{(P)}u^{(s,P)}\|_1\\ &\quad + \Big\|\nabla\cdot e^f\|_0\|\nabla\cdot\Big(u^{f,P} - Q_h^{(P)}\Big)u^{(f,P)}\Big)\|_0 + \|e^f\|_0\|u^f - Q_h^{(P)}u^{(f,P)}\|_0\Big)\\ &\quad + C_9(\omega)h\big(\|e^s\|_1\|u^{(s,P)}\|_2 + \|\nabla\cdot e^f\|_0\|\nabla\cdot u^{(f,P)}\|_1 + \|e^f\|_0\|u^{(f,P)}\|_1\big).\end{aligned} \tag{47}$$

Hence, apply the approximating properties (37) in (47) to obtain

$$\begin{aligned}&C_4\Big(\|e^s\|_1^2 + \|e^f\|_0^2 + \|\nabla\cdot e^f\|_0^2\Big)\\ &\leqslant C_{10}(\omega)\Big(h^2\Big[\|u^{(s,P)}\|_2^2 + \|u^{(f,P)}\|_1^2 + \|\nabla\cdot u^{(f,P)}\|_1^2\Big]\\ &\quad + \delta\Big[\|e^s\|_1^2 + \|e^f\|_0^2 + \|\nabla\cdot e^f\|_1^2\Big]\Big).\end{aligned} \tag{48}$$

Finally take δ small in (48) to obtain the estimate

$$\|e^s\|_1 + \|e^f\|_0 + \|\nabla\cdot e^f\|_0 \leqslant C_{11}(\omega)h\big(\|u^{(s,P)}\|_2 + \|u^{(f,P)}\|_1 + \|\nabla\cdot u^{(f,P)}\|_1\big). \tag{49}$$

With identical argument, estimate (49) can be derived for the error $\widetilde{e} = u^{(h,T)} - u^{(T)}$.

Thus we conclude the validity of the following theorem.

Theorem 3. *The solutions $u^{(h,P)}, u^{(h,T)}$ of problems (38) and (39) satisfy the following a priori error estimates*

$$\begin{aligned}&\|u^{(s,h,j)} - u^{(s,j)}\|_1 + \|u^{(f,h,j)} - u^{(f,j)}\|_0 + \|\nabla\cdot\big(u^{(f,h,j)} - u^{(s,j)}\big)\|_0\\ &\quad\leqslant C_{11}(\omega)h\big(\|u^{(s,j)}\|_2 + \|u^{(f,j)}\|_1 + \|\nabla\cdot u^{(f,j)}\|_1\big), \quad j = P,T.\end{aligned} \tag{50}$$

for any $\omega > 0$ satisfying the condition (41).

6. A Monte Carlo approach for stochastic fractal parameter distributions

A precise knowledge of the spatial distribution of the rock heterogeneities at mesoscopic scales may not be feasible. Instead, they can be represented as stochastic functions (parameters) with given spectral density distributions. In this sense, to obtain significant values for the *effective* complex moduli in highly heterogeneous fluid-saturated porous media, we propose to apply the numerical *gedanken* experiments in a Monte Carlo fashion. Thus, the compressibility and shear tests are applied to representative volumes of bulk material containing stochastic heterogeneities characterized by fractal spectral density distributions, and the boundary value problems are solved for each realization. The means and variances of the phase velocities and inverse quality factors associated with the complex moduli are obtained by averaging over realizations of the stochastic parameters, and they represent the statistical behavior of the response of the porous rocks under consideration.

The generation of these kind of heterogeneities involves the use of a stochastic fractal field, based on the so-called von Karman self-similar correlation functions. These models are widely used in the statistical characterization of heterogeneities for different applications.

Following [9] and more recently [21], we consider a particular case for which the spectral density of the stochastic field is given by:

$$S_d(k_x,k_y) = S_0(1 + k^2a^2)^{-(H+E/2)} \tag{51}$$

where $k = \sqrt{k_x^2 + k_y^2}$ is the radial wavenumber, a the correlation length, H is a self-similarity coefficient $(0 < H < 1)$ and S_0 is a normalization constant. Eq. (51) corresponds to a fractal process of dimension $D = E + 1 - H$ at scales smaller than a.

For a given realization of the stochastic parameters, the numerical problem (5) with either (6)–(11) or (15)–(17) as boundary conditions was solved for a finite number of frequencies $\omega_m, m = 1,\ldots,N_F$ in the range of interest, from where the values of $V_p^n(\omega_m), V_s^n(\omega_m), 1/Q_p^n(\omega_m)$ and $1/Q_s^n(\omega_m)$ were obtained. This procedure was repeated for a large number of realizations $n = 1,\ldots,N_R$, and the statistical behavior of the phase velocities and inverse quality factors after N_R realizations was analyzed by computing the mean and variance of these quantities in the form:

$$\langle\beta(\omega_m,N_R)\rangle = \frac{1}{N_R}\sum_{n=1}^{N_R}\beta^n(\omega_m), \quad \beta = V_p, V_s, 1/Q_p, 1/Q_s, \tag{52}$$

$$\sigma_\beta^2(\omega_m,N_R) = \frac{1}{(N_R-1)}\sum_{n=1}^{N_R}[\beta^n(\omega_m) - \langle\beta(\omega_m,N_R)\rangle]^2. \tag{53}$$

To analyze the convergence of the Monte Carlo approach in terms of the number of realizations N_R, the frequency average of the variances was computed by

$$\|\sigma_\beta^2(N_R)\| = \left[\frac{1}{N_F}\sum_{j=1}^{N_F}\sigma_\beta^2(\omega_j,N_R)\right]^{1/2}, \quad \beta = V_p, V_s, 1/Q_p, 1/Q_s. \tag{54}$$

As indicated before, the Monte Carlo simulations were stopped when the variance (54) of the computed quantities stabilized at an approximate constant value defined in terms of a given tolerance.

Remark 1. The size of the representative volume, i.e. the computational domain to be used in the numerical experiments, is not arbitrary: the side length L has to be big enough to contain a significant number of mesoscopic scale heterogeneities but, at the same time, it has to be much smaller than the wavelengths associated with each excitation frequency. To find an upper bound for L we checked that the compressibility and shear tests applied to homogeneous samples of side length L, composed of any of the different materials forming the heterogeneous medium, give negligible attenuation and velocity dispersion in the frequency range under consideration.

7. Numerical experiments

7.1. Validation of the procedure

First, to validate the proposed methodology, Figs. 1 and 2 display the results of the compressibility test to obtain the P-wave phase velocities and inverse of quality factors for the case in which the sample is a periodic media consisting of alternating layers of equal thickness 0.2 m saturated with either gas or water. The physical properties of the solid matrix are taken constant in all the domain, and correspond to the sandstone 1 in Table 1, while the physical properties of the fluids (water and gas) are given in Table 2. We compare the phase velocities and inverse quality factors obtained using our numerical approach for frequencies between 0 and 100 Hz with the corresponding values calculated as indicated in Appendix A using the theory of [23] but, in the last case, considering a periodic medium composed of alternating layers of equal thickness 0.4 m saturated with either gas or water. This comparison is valid because the boundary conditions (6)–(11) for the compressibility test can be associated with a compression similar to that proposed by [23], but applied to a periodic sample obtained by a mirror reflection with respect to the x-axis of the domain Ω. As can be observed in Figs. 1 and 2, the computed values are in excellent agreement with those predicted by White's theory.

In the case of the shear modulus and for uniform either gas or water saturation, the code was checked to yield the real shear modulus at the zero limit frequency.

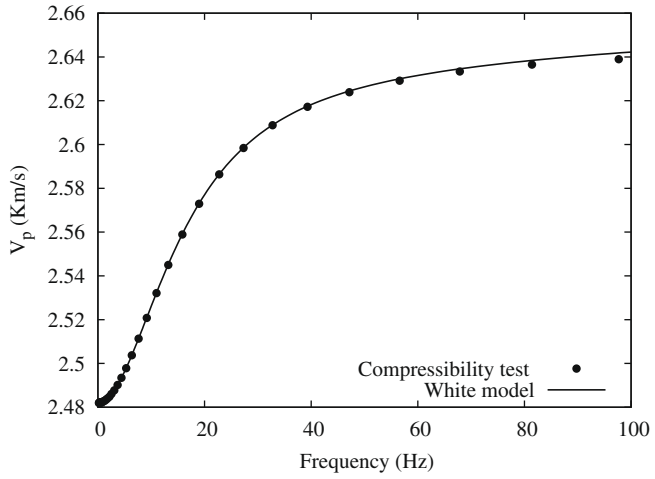

Fig. 1. P-wave phase velocity obtained from the compressibility test (dots) and using White's theory (line) for frequencies lying between 0 and 100 Hz.

Table 1
Physical properties of the solid materials used in the numerical examples.

	Sandstone 1	Sandstone 2	Shale
K_s	37 GPa	37 GPa	25 GPa
ρ_s	2650 kg/m^3	2650 kg/m^3	2550 kg/m^3
ϕ	0.3	0.2	0.3
K_m	4.8 GPa	12.1 GPa	3.3 GPa
μ	5.7 GPa	14.4 GPa	1.2 GPa
k	1 Darcy	0.23 Darcy	1.5×10^{-5} Darcy

Table 2
Physical properties of the fluids used in the numerical examples.

	Water	Gas
K_f	2.25 GPa	0.012 GPa
ρ_f	1040 kg/m^3	78 kg/m^3
η	0.003 Pa s	0.00015 Pa s

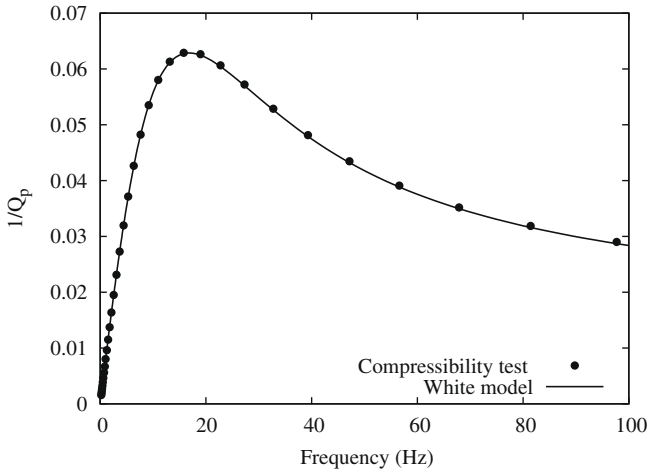

Fig. 2. P-wave inverse quality factor obtained from the compressibility test (dots) and using White's theory (line) for frequencies lying between 0 and 100 Hz.

7.2. The patchy gas–water saturation case

An interesting case arise in hydrocarbon reservoirs, where regions of non-uniform patchy saturation occur at gas–water contacts. Patchy saturation patterns produce very important mesoscopic effects at the seismic band of frequencies, as shown by White in [22].

In order to study these effects, we consider porous samples with spatially variable gas–water distribution in the form of irregular patches fully saturated with gas and zones fully saturated with water. We consider that the domain Ω is a square of side length 20 cm, and the partition $\mathscr{T}^h$ is composed of 75×75 squares Ω_j. For each computation, the excitation frequency is varied from 0 to 900 Hz using $N_f = 20$ equally spaced values. The solid matrix is the sandstone 1 with properties given in Table 1, while the physical parameters of the fluids are those given in Table 2.

To generate realizations of this type of binary fluid distributions we proceed as follows. The first step to generate a patchy fluid distribution is to assign to each subdomain Ω_j of the partition $\mathscr{T}^h$ a pseudo-random number using a generator with uniform distribution associated to a given *seed* number. This random field is Fourier transformed to the spatial wavenumber domain and its amplitude spectrum is filtered using Eq. (51). The result is then transformed back to the spatial domain, obtaining a *micro-heterogeneous* water saturation model $S_w^{(j)}, j = 1, \ldots, J$.

Next, to assign to each cell Ω_j pure water or pure gas, we choose a threshold value S^* so that for each subdomain Ω_j where $S_w^{(j)} \leqslant S^*$ we assume that such subdomain is fully saturated with gas, while if $S_w^{(j)} > S^*$ we consider that Ω_j is fully saturated with water. In this way, the patchy saturation model is constructed and an overall water saturation $\overline{S}_w$ is obtained for the computational rock sample.

We analyze a set of experiments involving $N_R = 70$ realizations, choosing S^* in each case so that the overall gas saturation $(1 - \overline{S}_w)$ of the 70 realizations are fixed and equal to 0.1. The correlation length a is taken to be 4 cm. An example of the gas–water distribution for a particular realization is illustrated in Fig. 3, where the black zones correspond to pure gas saturation and the white ones to pure water saturation.

To illustrate the loss mechanism being analyzed, Fig. 4 shows the normalized fluid-pressure amplitude field induced by the compressibility experiment at a frequency of 190 Hz for the particular realization shown in Fig. 3. Comparing Figs. 3 and 4 it can be seen that the compressibility test induces greater fluid pressures in the water-saturated zones than in the gas-saturated ones, which is related to the fact that the bulk modulus of the gas is much smaller than that of the water. The associated fluid-pressure gradient, which has its greatest values in the interfaces between the zones fully saturated with gas and those fully saturated with water, produces fluid flow and Biot slow waves which difusse away from the gas–water interfaces generating energy losses and velocity dispersion on the fast compressional waves.

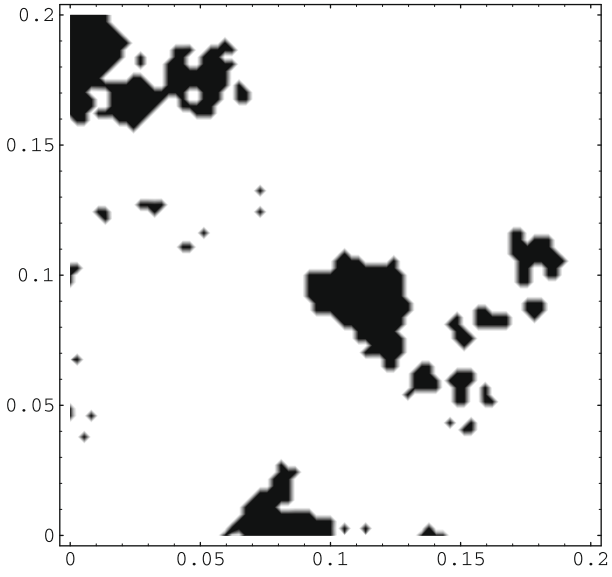

Fig. 3. Gas–water distribution for a given realization. Black zones correspond to pure gas saturation and the white ones to pure water saturation. The overall gas saturation is 0.1.

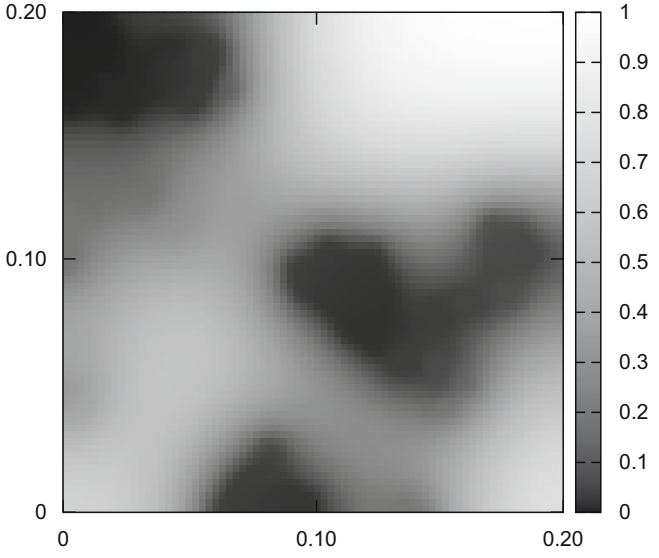

Fig. 4. Normalized fluid-pressure amplitude for the fluid distribution shown in Fig. 3. The excitation frequency is 190 Hz.

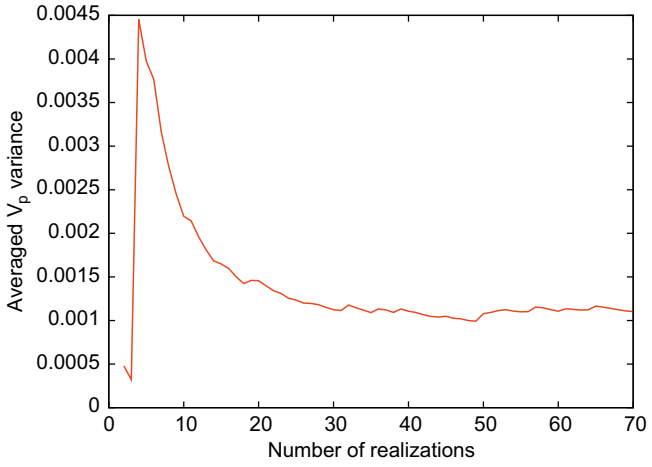

Fig. 5. Averaged variance of the compressional phase velocity as function of the total number of realizations.

Next, we show the results of applying the Monte Carlo procedure to determine the *effective* complex moduli for patchy saturation distributions. Fig. 5 shows the variance of the compressional phase velocity averaged in the whole range of frequencies for different values of N_R. It can be observed that after 70 realizations this parameter stabilizes at an almost constant value, with a similar behavior observed for the inverse quality factor. This fact suggests that the *effective* compressional velocity and inverse quality factor as a function of frequency, defined as the mean compressional velocity and mean compressional inverse quality factor after 70 realizations as shown in the next two figures are representative physical parameters for the kind of media under consideration.

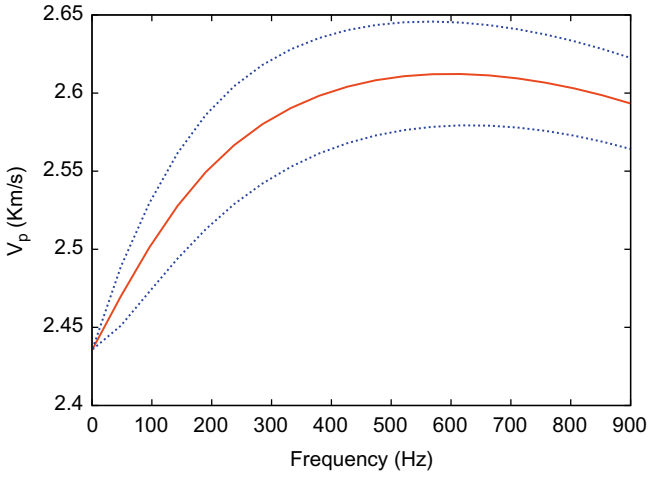

Fig. 6. Effective compressional phase velocity as function of frequency (solid lines). Dotted lines indicate the corresponding standard deviations.

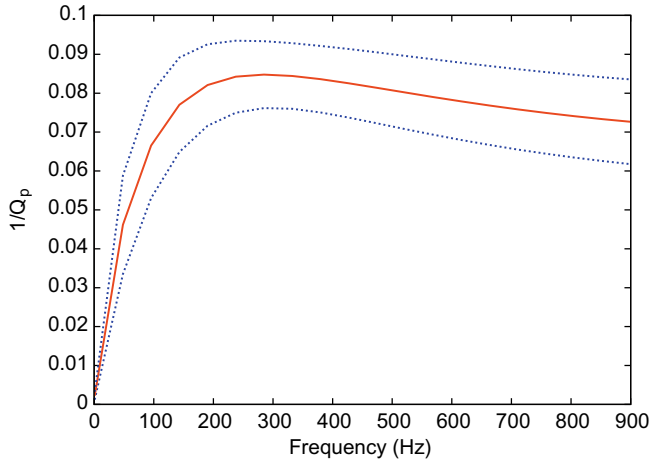

Fig. 7. Effective compressional inverse quality factor as function of frequency. Dotted lines indicate the corresponding standard deviations.

Fig. 6 displays the mean compressional velocity versus frequency after 70 realizations and their corresponding standard deviation (which are indicated with dotted lines). We observe an important dispersion of the compressional phase velocity in the whole frequency range. Fig. 7 illustrates the behavior of the mean compressional inverse quality factor versus frequency and their corresponding standard deviation; we can see that the mesoscopic attenuation is very important for almost all the frequency range under consideration, with a maximum value of about 12 at 250 Hz showing the drastic amplitude losses that would suffer compressional waves propagating through these kind of media.

In order to obtain the effective complex shear modulus of these samples we also applied the shear tests to the same set of patchy-saturated rocks. As expected, the effective shear modulus resulted to have negligible imaginary part, while its real part was very close to the shear modulus of the dry matrix. This behavior is due to the fact that shear tests applied to samples where the heterogeneities are related to fluid inhomogeneities induce negligible values of the fluid-pressure gradient and, thus, negligible mesoscopic effects.

7.3. The shale–sandstone mixture case

The finite element procedures (38) and (39) were implemented to analyze the response of a rock sample composed of a mixture of two different materials: the sandstone 2 of Table 1, fully saturated with gas and shale (with properties given in the same Table), fully saturated with water. We consider that the domain Ω is a square domain of side length 1 cm, and the partition $\mathscr{T}^h$ is composed of 75×75 squares Ω_j. For each realization, the boundary value problems associated with the compressibility and shear tests were solved for $N_f = 20$ frequencies in the range 0 to 5000 Hz.

We assume a distribution of shale and sandstone in the form of irregular patches following the stochastic fractal field based on the von Karman self-similar correlation functions as explained above. The procedure to generate the mixture is similar to that explained for the case of patchy saturation. We assign to each subdomain Ω_j a pseudo-random number using a generator with uniform distribution. This random field is Fourier transformed to the spatial wavenumber domain and its amplitude spectrum is filtered using Eq. (51). The result is then transformed back to the spatial domain, obtaining a *micro-heterogeneous* sandstone content model $S^{(j)}, j = 1, \cdots, J$.

Next, to assign to the matrix of each Ω_j pure shale or pure sandstone, we choose a threshold value S^* so that for each subdomain Ω_j where $S^{(j)} \leqslant S^*$ we assume that such subdomain matrix is pure shale, while if $S^{(j)} > S^*$ we consider that Ω_j is pure sandstone. In this way, the highly heterogeneous mixture model is constructed and an overall sandstone content $\overline{S}$ is obtained for the computational rock sample. In this experiment we choose S^* so that the overall sandstone content $\overline{S}$ is equal to 0.5. The parameters of the fractal spectral density are respectively $E = 2, D = 2.2$ and the correlation length a is taken to be 7×10^{-3} cm. The distribution of shale and sandstone obtained in this fashion is illustrated in Fig. 8, where the black zones correspond to pure shale while the white ones to pure sandstone.

These combined lithological and fluid variations produce strong mesoscopic effects in the case of the compressibility tests, as it is shown in Figs. 9 and 10 where the *equivalent* compressional phase velocity and inverse quality factor for the particular realization shown in Fig. 8 are plotted as function of frequency; we can see that for frequencies around 750 Hz the quality factor Q_p takes very low values of about 8, while the compressional velocity shows a high velocity dispersion, with about 18% increase between 0 and 5000 Hz.

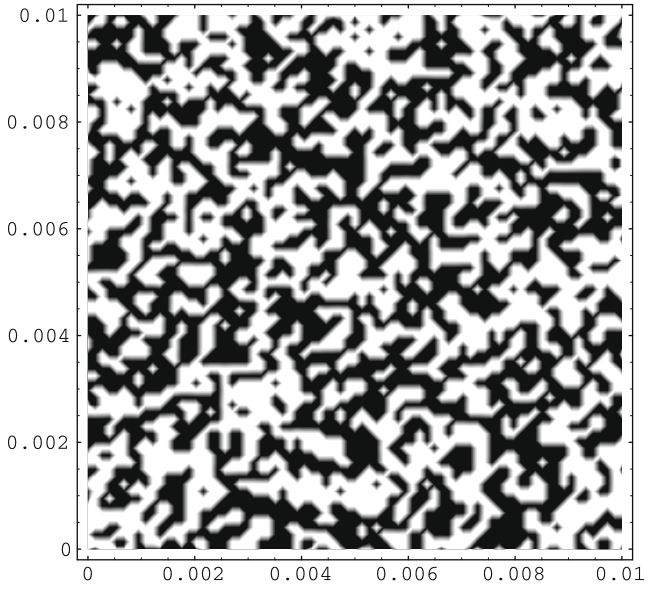

Fig. 8. Distribution of shale and sandstone. Black zones correspond to pure shale, and the white ones to pure sandstone.

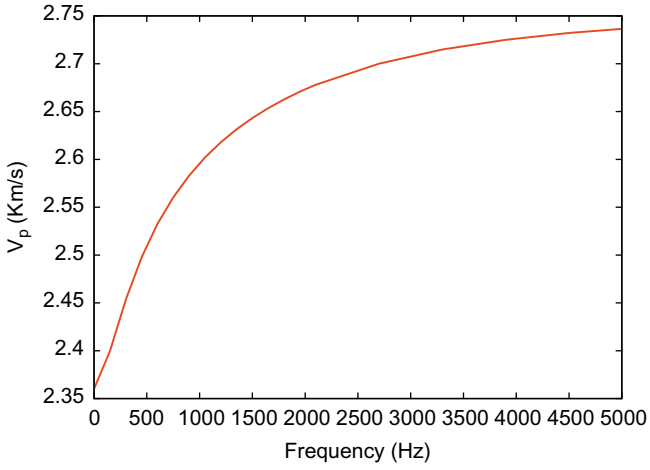

Fig. 9. Equivalent P-wave phase velocity as function of frequency.

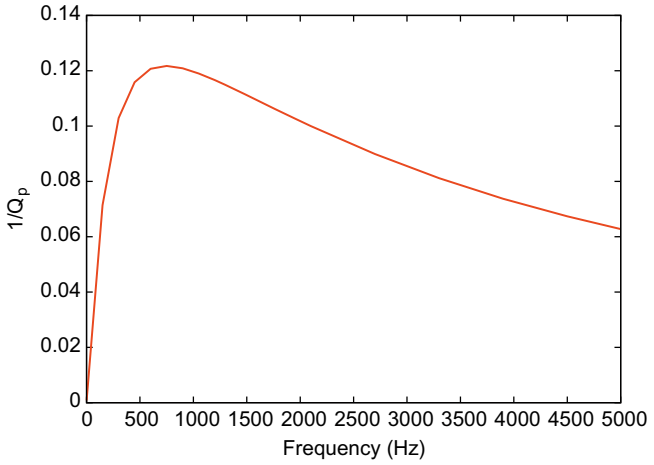

Fig. 10. Equivalent compressional inverse quality factor as function of frequency.

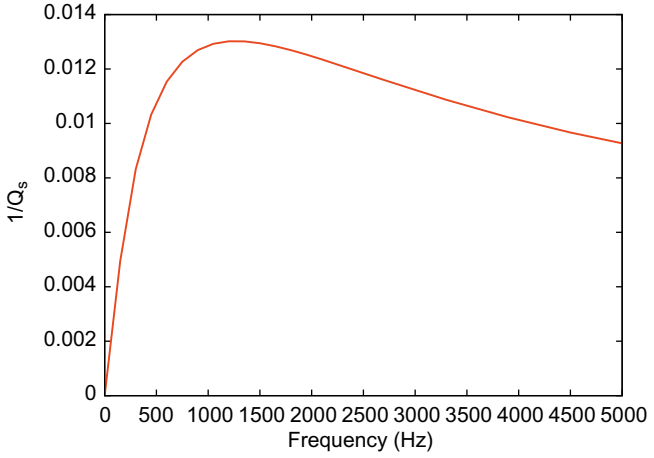

Fig. 11. Equivalent shear inverse quality factor as function of frequency.

These mesoscopic scale heterogeneities also produce non-negligible mesoscopic effects in the case of the quasistatic shear tests. In fact, Fig. 11 shows the shear inverse quality factor as function of the frequency. It can be seen that the lithological variations produce non-negligible effects, with values of Q_s of about 75 for a frequency of 1200 Hz. This fact is showing us that shear waves propagating through these kind of media are also affected by wave-induced fluid flow effects. The associated *equivalent* shear velocity shows very slight dispersion, being approximately equal to 1.3 Km/s in the whole range analyzed. We do not include the corresponding Figure for brevity. The Monte Carlo simulation procedure was performed for this particular set of stochastic parameters by generating a set of realizations, but since in the range of frequencies being analyzed the rock samples are statistically homogeneous the variances of the phase velocities and inverse quality factors show negligible values. Thus we may conclude that the values determined from the chosen realization are associated with an *effective* viscoelastic medium having in the average the same response than our highly heterogeneous fluid-saturated porous medium.

8. Conclusions

In this paper we presented a numerical upscaling procedure to estimate the *effective* phase velocity and quality factors in highly heterogenous fluid-saturated porous rocks, with heterogeneities represented by stochastic fractals.

The methodology is based on the finite element solution of the classical Biot's equations to simulate oscillatory compressibility and shear tests, combined with a Monte Carlo approach to obtain the complex *effective* compressional and shear phase velocities and inverse quality factors in this type of media.

Unlike the analytical White's theories ([23,22]) valid only for periodic alternating layers or for spherical gas pockets, our method allows to simulate any kind of heterogeneities in the solid matrix and the saturant fluids within the domain.

In order to illustrate the procedure, numerical experiments were performed to obtain the effective complex moduli in gas–water patchy-saturated sandstones and in partially saturated mixtures of sandstone and shale at frequencies ranging from the seismic to the sonic range. We concluded that mesoscopic attenuation and velocity dispersion can be very important in the case of compressional waves propagating in patchy-saturated media in the range 0 to 900 Hz. Also, we showed that mesoscopic scale lithological variations in partially saturated rocks can produce non-negligible mesoscopic effects in the propagation of shear and compressional waves in the range 0 to 5 kHz.

The presented numerical upscaling procedure may be used to replace a highly heterogeneous porous medium with stochastic heterogeneities characterized by a given spectral density distribution by an *effective* viscoelastic medium behaving in the average as the original medium. The computational advantages of this methodology are obvious due to the drastic reduction in the number of degrees of freedom needed to represent the obtained *effective* viscoelastic medium as compared with the original heterogenous one and will be the subject of forthcoming works.

Acknowledgements

This work was partially supported through Grant PICT 03-13376 from the Agencia Nacional de Promoción Científica y Tecnológica, Argentina (ANPCyT) and from Grant PIP 04-5126 from CONICET, Argentina.

Appendix A. Calculation of the complex plane wave modulus in a periodic system of fluid-saturated porous layers

We consider a periodic layered system composed of porous media 1 and 2 with thickness $d_l, l = 1, 2$ and period $d_1 + d_2$. White et al. [23] obtained the complex *undrained* plane wave modulus $\widetilde{M}(\omega)$ for a fast P1 wave traveling along the direction perpendicular to the stratification. It is given by

$$\widetilde{M}(\omega) = \left[\frac{1}{M_0} + \frac{2(r_2 - r_1)^2}{i\omega(d_1 + d_2)(l_1 + l_2)}\right]^{-1}, \tag{55}$$

where

$$M_0 = \left(\frac{p_1}{M_{G_1}} + \frac{p_2}{M_{G_2}}\right)^{-1}, \tag{56}$$

with $p_l = d_l/(d_1 + d_2), l = 1, 2$. Omitting the subindex l for clarity, we have for each medium

$$M_G = K_c + \frac{4}{3}\mu, \tag{57}$$

where K_c is given by Eq. (3).

Moreover,

$$r = \frac{\alpha K_{av}}{M_G} \tag{58}$$

is the ratio of fast P-wave fluid tension to total normal stress,

$$I = \frac{\eta}{kq}\coth\left(\frac{kd}{2}\right) \tag{59}$$

is an impedance related to the slow P-wave,

$$q = \sqrt{\frac{i\omega\eta}{kK_E}} \tag{60}$$

is the complex wavenumber of the slow P-wave and

$$K_E = \frac{M_{dry}K_{av}}{M_G}, \tag{61}$$

is an effective modulus, with

$$M_{dry} = K_m + \frac{4}{3}\mu \tag{62}$$

being the dry-rock fast P-wave modulus.

References

[1] M.A. Biot, Theory of propagation of elastic waves in a fluid-saturated porous solid. I. Low frequency range, J. Acoust. Soc. Am. 28 (1956) 168–171.
[2] M.A. Biot, Theory of propagation of elastic waves in a fluid-saturated porous solid. II. High frequency range, J. Acoust. Soc. Am. 28 (1956) 179–191.
[3] M.A. Biot, Mechanics of deformation and acoustic propagation in porous media, J. Appl. Phys. 33 (1962) 1482–1498.
[4] T. Cadoret, D. Marion, B. Zinszner, Influence of frequency and fluid distribution on elastic waves velocities in partially saturated limestones, J. Geophys. Res. 100 (1995) 9789–9803.
[5] J.M. Carcione, S. Picotti, P-wave seismic attenuation by slow-wave diffusion: effects of inhomogeneous rock properties, Geophysics 71 (2006) 01–08.
[6] P.G. Ciarlet, The Finite Element Method for Elliptic Problems, North Holland, 1980.
[7] J. Douglas Jr, F. Furtado, F. Pereira, The statistical behavior of instabilities in immiscible displacement subject to fractal geology, in: A. Burgeaut, C. Carasso, S. Luckhaus, A. Mikelic (Eds.), Mathematical Modeling of Flow Through Porous Media, World Scientific, Singapore, 1997, pp. 115–137.
[8] N.C. Dutta, H. Odé, Attenuation and dispersion of compressional waves in fluid-filled porous rocks with partial gas saturation (White model). Part I: Biot theory, Geophysics 44 (11) (1979) 1777–1788.
[9] A. Frankel, R.W. Clayton, Finite difference simulation of seismic wave scattering: implications for the propagation of short period seismic waves in the crust and models of crustal heterogeneity, J. Geophys. Res. 91 (1986) 6465–6489.
[10] F. Gassmann, Über die elastizität poröser medien (“On the elasticity of porous media”), Vierteljahrsschrift der Naturforschenden Gessellschaft in Zurich 96 (1951) 1–23.
[11] L. Guarracino, J.E. Santos, Stochastic modeling of variably saturated flow in fractal porous media, Math. Geol. 36 (2) (2004) 239–260.
[12] H.B. Helle, N.H. Pham, J.M. Carcione, Velocity and attenuation in partially saturated rocks – Poroelastic numerical experiments, Geophys. Prospect. 51 (2003) 551–566.
[13] H. Kolsky, Stress Waves in Solids, Dover publications, New York, 1963.
[14] Y. Mason, S. Pride, Poroelastic finite difference modeling of seismic attenuation and dispersion due to mesoscopic-scale heterogeneity, J. Geophys. Res. 112, B03204.
[15] J.C. Nedelec, Mixed finite elements in R^3, Numer. Math. 35 (1980) 315–341.
[16] J.A. Nitsche, On Korn’s second inequality, RAIRO 15 (1981) 237–249.
[17] S. Pride, E. Tromeur, J.G. Berryman, Biot slow-wave effects in stratified rock, Geophysics 67 (2002) 271–281.
[18] P.A. Raviart, J.M. Thomas, Mixed finite element method for 2nd order elliptic problems, Mathematical Aspects of the Finite Element Methods, Lecture Notes of Mathematics, vol. 606, Springer, 1975.
[19] J.G. Rubino, J.E. Santos, S. Picotti, J.M. Carcione, Simulation of upscaling effects due to wave-induced fluid flow in Biot media using the finite element methods, J. Appl. Geophys. 62 (2007) 193–203.
[20] J.E. Santos, J.M. Corbero, C.L. Ravazzoli, J.L. Hensley, Reflection and transmission coefficients in fluid-saturated porous media, J. Acoust. Soc. Am. 91 (4) (1992) 1911–1923.
[21] J.E. Santos, C.L. Ravazzoli, P.M. Gauzellino, J.M. Carcione, Numerical simulation of ultrasonic waves in reservoir rocks with patchy saturation and fractal petrophysical properties, Comput. Geosci. 9 (2005) 1–27.
[22] J.E. White, Computed seismic speeds and attenuation in rocks with partial gas saturation, Geophysics 40 (1975) 224–232.
[23] J.E. White, N.G. Mikhaylova, F.M. Lyakhovitskiy, Low-frequency seismic waves in fluid-saturated layered rocks, Izvestija Academy of Sciences USSR, Phys. Solid Earth 10 (1975) 654–659.